Combining video telemetry and wearable MEG for naturalistic imaging

George C. O'Neill[a,b,*], Robert A. Seymour[a], Stephanie Mellor[a], Nicholas Alexander[a], Tim M. Tierney[a], Léa Bernachot[a], Mansoureh Fahimi Hnazaee[a], Meaghan E. Spedden[a], Ryan C. Timms[a], Sven Bestmann[a,c], Matthew J. Brookes[d], Gareth R. Barnes[a]

[a]*Wellcome Centre for Human Neuroimaging, Department of Imaging Neuroscience, UCL Queen Square Institute of Neurology, University College London, London, UK*
[b]*Department of Neuroscience, Physiology and Pharmacology, University College London, London, UK*
[c]*Department of Clinical and Movement Neurosciences, UCL Queen Square Institute of Neurology, University College London, London, UK*
[d]*Sir Peter Mansfield Imaging Centre, School of Physics and Astronomy, University of Nottingham, Nottingham, UK*

Abstract

Neuroimaging studies have typically relied on rigorously controlled experimental paradigms to probe cognition, in which movement is primitive, an afterthought or merely used to indicate a subject's choice. Whilst powerful, these paradigms often do not resemble how we behave in everyday life, so a new generation of ecologically valid experiments are being developed. Magnetoencephalography (MEG) measures neural activity by sensing extracranial magnetic fields. It has recently been transformed from a large, static imaging modality to a wearable method where participants can freely move. This makes wearable MEG systems a candidate for naturalistic experiments going forward.

Additional measures that capture information about complex behaviours that are compatible with neuroimaging techniques, such as MEG, will benefit researchers therefore needed for naturalistic experiments using naturalistic paradigms. Here we use video data from multi-limb dance moves, processed with open-source machine learning methods, to directly cue the timings of task onset and offset in wearable MEG data In a first step, we compare a traditional, block-designed analysis of limb movements, where the times of interest are based on stimulus presentation, to an analysis pipeline based on hidden Markov model states derived from the video telemetry. We then show that by observing the participants choreographed movement in a dancing paradigm, it is possible to express modes of neuronal activity related to specific limbs and body posture. This demonstrates the potential of combing video telemetry with mobile neuroimaging for future studies of complex and naturalistic behaviours.

*Corresponding author:
George C. O'Neill: g.o'neill@ucl.ac.uk

This is a preprint submission to bioRxiv, which may not reflect the final version of the manuscript.

1) Introduction

One of the challenges for neuroimaging is the development of more *naturalistic* and ecologically valid approaches for studying brain function (Finn et al., 2022). Much effort has been made in creating experimental environments, such as complex stimuli to assess brain function in a way which is closer to the real world than the laboratory (Betti et al., 2013; Kim et al., 2018; Kringelbach et al., 2023). However, a fundamental limitation remains in that the actual expression of behaviour through movement is limited in most neuroimaging modalities. This, ultimately, limits the ecological validity of studies of brain function, where movement is often merely an afterthought.

Magnetoencephalography (MEG; Cohen, 1972; Hämäläinen et al., 1993) is a powerful non-invasive method of imaging neural function from the brain, which measures the changes in extracranial magnetic field originating from dendritic current flow. As MEG is a direct measure of underlying neural processes it offers a millisecond scale temporal resolution to capture the rapid dynamics of cognition. Furthermore, unlike electroencephalography (EEG) which measures the same signal via electric potentials on the scalp, the magnetic fields pass through the skull with relatively little distortion and so MEG offers a high spatial resolution when the data are source-reconstructed. However, magnetic fields from neural populations in the brain are of the order of 10s of femtoTesla, so traditional MEG systems have required an array of highly sensitive superconducting sensors and the cumbersome cryogenic infrastructure that supports them. The resultant form factor of the cryogenic MEG system means participants have to keep their head (and by extension, the rest of their body) as still as possible within a gantry which contains the sensing array. Whilst naturalistic MEG studies exist (e.g. listening to speech or watching movies (Betti et al., 2013; Nunes et al., 2020; Park et al., 2016; Thiede et al., 2020)), the constraint on movement makes these studies passive, with participants not behaving in a natural way during the presentation of the stimulus.

Recent advances in the engineering of cryogen-free sensors, particularly optically pumped magnetometers (OPMs; Knappe et al., 2016; Osborne et al., 2018; Shah and Wakai, 2013; Sheng et al., 2017) have led to the rapid development of a new generation of optically pumped (OP) MEG systems (Borna et al., 2017; Boto et al., 2017; Iivanainen et al., 2019; Pratt et al., 2021). OP-MEG has been demonstrated to be practical in assessing sensory (Hill et al., 2019; Roberts et al., 2019; Seymour et al., 2021a) and cognitive processes (Barry et al., 2019; de Lange et al., 2021; Rhodes et al., 2023; Tierney et al., 2018), as well as showing its potential for clinical applications (Feys et al., 2023, 2022; Hillebrand et al., 2023; Vivekananda et al., 2020). Their diminutive size (commercial OPMs are approximately the size of a 2-by-3 LEGO brick) mean many of these sensors can be packed into a rigid helmet (Boto et al., 2017) or soft cap (Feys et al., 2022; Hill et al., 2020), close to the scalp and worn in a form factor similar to an EEG. A further advantage of this wearable MEG system over EEG is the fact that muscle activity from the neck or other body parts do not contaminate the MEG signal to the same proportion as in EEG (Boto et al., 2019; Muthukumaraswamy, 2013), which can prove highly beneficial if a study requires explicit movement. It is for these reasons that OP-MEG promises to be a powerful tool in the field of naturalistic imaging (Stangl et al., 2023), as well as having already demonstrated compatibility with immersive virtual reality environments (Roberts et al., 2019) and reliably imaging neural processes whilst moving large (> 1 m) distances (Holmes et al., 2023b; Mellor et al., 2023; Seymour et al., 2021a), whilst two subjects play a ball-game against each other (Holmes et al., 2023a), or simply drinking tea (Boto et al., 2018) OP-MEG can therefore be conducted, in principle, during unconstrained movement, a critical step towards realistic and ecologically valid neuroimaging.

One challenge is how to incorporate subject behaviour into our modelling of neuroimaging data as experiments become increasingly realistic and complex (Stangl et al., 2023). Recent developments in computer vision and machine learning methods to track behaviour is a promising approach which we chose to employ (Anderson and Perona, 2014; Mathis et al., 2018; Schneider et al., 2023; Weinreb et al., 2023). Here, we showcase how behavioural information that is extracted from data-mined video of participants performing complex motor paradigms can be fused with the concurrently recorded wearable MEG data to yield brain activity maps of complex behaviour. We first show that in a simple proof of principle study we can decode the experimental condition of the participant through the video data alone. Next, we show that by using the video, we can return context to MEG data from participants dancing and use the video-derived cues to quantify neuronal activity associated with specific limbs or postures.

2) Methods

2.1) Experiment

This study was collected at the OP-MEG scanning suite at the Wellcome Centre for Human Neuroimaging. The project was approved by the University College London research ethics committee. All participants who took part in the study providing informed written consent prior to MEG/MRI data collection.

Motor block design

One participant (male, aged 27) took part in a motor paradigm. Seated in the middle of the magnetic shielded room (MSR), the participant was visually cued to move one of their four limbs freely until a fixation cross appeared on the screen. The movement epochs were 4 s in length with a 10–11 s inter trial interval. In a block, 15 trials of each condition were presented in a pseudorandom order, with two blocks recorded.

Dancing

4 participants (all male, aged 34±14 [mean±SD years]) danced the *Hokey Cokey*, a popular dance for school children in the United Kingdom. It was selected as its major actions involve moving individual limbs separately, with periods where the lyrics explicitly instruct the dancer how to move ("you put your left arm in…") as well as periods of ambiguity ("whoa, the Hokey Cokey!"). Instructions for a basic choreography were given prior to recording. An audio recording of the song (Black Lace, 1985) was played into the room from a set of speakers placed outside of the room. Subjects repeated the dance multiple times. In total 15 recorded dances were kept for further analysis.

2.2) Acquisition

Magnetic Resonance Imaging

Each participant underwent Magnetic Resonance Imaging (MRI) in preparation for the study on a Tim Trio 3T MR System (Siemens Healthineers, Erlangen, Germany). Two images were acquired for each participant. The first, a modified FLASH sequence with a high-bandwidth readout (FOV: 256 mm (A-P) x 256 mm (S-I) x 192 mm (L-R); resolution 1 mm x 1 mm x 1 mm) for minimal distortion of the participants' face and scalp, whilst maintaining enough dynamic range to segment white and grey matter in the brain. Full details of the acquisition parameters can be found in Meyer et al., (2017). The second, a T1-weighted image (MPRAGE; TR=2530 ms, TE=3.34 ms; FOV: 256 mm (A-P) x 256 mm (S-I) x 172 mm (L-R); resolution 1 mm x 1 mm x 1 mm) was collected to supplement the first scan, in case automatic segmentation methods with the FLASH MR image failed.

MEG

For both experiments a bespoke scanner-cast to hold an array of OPMs was created from each participant's MRI, which allowed the OPMs to be worn directly on the scalp and allowed recording of MEG during large participant movements within the scanning environment (Mellor et al., 2023; Seymour et al., 2021b).

The OPM array consisted of a combination of 2nd generation (dual axis) and 3rd generation (triaxial) zero-field magnetometers (QuSpin, Louisville, CO). The dual axis sensors provided axial-oriented field detection and one tangential field measure, the triaxials give a full vector field measurement. The sensors operated in a gain mode with a dynamic range of ~±4.5 nT relative to their zero-field point. The number of sensors and channels placed on the scalp can be found in Table 1, and the sensor layouts are in the supplementary information. The MEG data were digitised using a 16-bit ADC system (National Instruments, Austin, TX) at a sample rate of 6000 Hz.

Subject	2nd Generation Sensors	3rd Generation Sensors	Total Channels
001	43	0	86
002	40	0	80
003	38	0	76
004	25	26	128

Table 1: Number of sensors and channels placed on the scalp for each participant. Each sensor provides one channel of axial-oriented field detection one tangential recording for 2nd generation sensors and a full vector measurement for the 3rd generation sensors.

The sensors were placed in bespoke 3D printed scanner-casts (Chalk Design, London, UK) specifically designed for each participant (Boto et al., 2017; Tierney et al., 2018) to ensure a comfortable fit and minimise the coregistration errors between the sensors and the participant's anatomy (Meyer et al., 2017). The helmet's geometry was based on a scalp mesh extracted from the FLASH MR images. The OPMs were oriented such that the manufacturer-defined Y-axis measured component of the magnetic field axial/radial to the scalp, with the centre of the vapour cell typically between 9 and 12 mm from the scalp surface. Sensor locations were *assumed* to be in the same coordinate system as the anatomical images.

MEG data were acquired in an MSR (Magnetic Shields Ltd, Staplehurst, UK), with internal dimensions of 4380 mm x 3380 mm x 2180 mm. The MSR is constructed from two inner layers of 1 mm mu-metal, a 6 mm copper layer, and then two external layers of 1.5 mm mu-metal. The room contains a series of built-in degaussing coils to minimise the residual background field in the room (Altarev et al., 2015). The degausser was used in the period after closing the participant in the room and prior to data acquisition. No active magnetic shielding was used for these experiments.

Video

Visible-light spectrum video recordings of the participants performing the experiments were recorded alongside the MEG data using a camera attached to a single-board computer (Raspberry Pi Foundation, Cambridge, UK). The camera was triggered to record via a GPIO pin controlled by the stimulus presentation software, sent to both the camera and the OPM acquisition electronics to allow for offline synchronisation. Video was recorded at a resolution of 640 x 480 pixels with a frame rate of 30 Hz (with the exception of subject 004, which was recorded at 50 Hz). The camera was located in front of 001, 002 and 004 (see Fig. 1 for an example), with the exception of subject 003, where the camera was placed approximately 45 degrees off axis to the right of the participant.

2.3) Preprocessing

Video

Telemetry information from the video was extracted using OpenPose (Cao et al., 2021), a pre-trained convolutional neural network which is capable of single and multi-person pose estimation from images and video. Inference was performed using an RTX A5000 GPU (NVIDIA, Santa Clara, CA), and for every frame, the X-Y pixel locations and a confidence-of-fit score for 25 different key-points of the body were recorded. An example of the keypoints fitted to each frame can be found in Figure 1. For each experiment, the telemetry position data was linear interpolated to fix missing data, was converted to speed (units: pixels / frame) and normalised via a Z-transform. Finally, the 50 Hz telemetry from subject 004, was linear interpolated to match the 30 Hz video sampling rate of subjects 001-003. For the dancing telemetry, each session's data were normalised individually and then concatenated in time. The data were then partitioned using a hidden Markov model (HMM), with a multivariate Gaussian mixture model used as the observation model, to derive when differing movement 'states' occurred in the data, HMM inference was handled with the HMM-MAR toolbox (Vidaurre et al., 2016) to separate the data into k states. On completion, the fitted HMM returned a probabilistic timeseries for each of the k states and Viterbi path which assigns a mutually-exclusive state on a per-frame basis.

In the block design experiment, we set $k = 10$. To identify what each state corresponded to, the binarised Viterbi path for a given state was compared to the initial block design timings, with the Jaccard index. The Jaccard index is a measure of the intersection of two sets relative to their union (Jaccard, 1912). The state with the highest Jaccard index for a given experimental condition was labelled with that condition name. The 6 remaining (unlabelled) states were considered as rest and combined into a single rest *meta-state*.

For the dancing experiment, where the video consisted a concatenated group of subjects (from different angles in the room) we inference on a $k = 25$ state HMM. The motivation for this was to assume that no two people would perform the movements in frame same way and so this would allow for multiple states corresponding to the same limb (but from different subjects) to be identified. After HMM fitting, the Viterbi paths were regressed against the telemetry of each key-point, to generate regression maps of movement (examples can be seen in Figures 2B and 4A). From these maps, which limb (or dance move) a state corresponded to was performed by visual inspection, with appropriate labelling of the states applied. If two or more states represented the same limb (but across different subjects), their Viterbi paths were pooled together to make one meta-state representing the limb across all subjects. The results of which state corresponds to which limb can be found in the supplementary information.

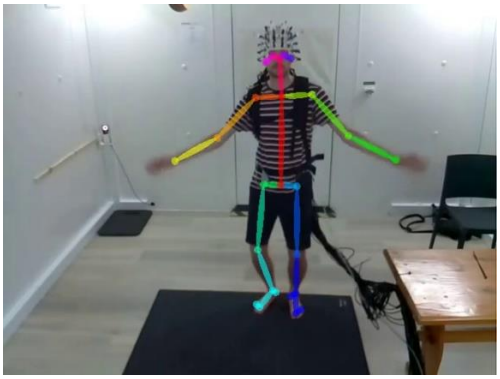

Figure 1: A subject performing the dancing paradigm within the magnetically shield room whilst wearing the MEG system. The pose estimation results for this video frame have been superimposed to represent where the keypoints (circles) used for telemetry analysis are located.

MEG

An anti-aliasing 500 Hz low-pass filter (60th order FIR filter combined with a Kaiser window) was applied to the MEG data and then downsampled to a sample rate of 2000 Hz. The HMM state time courses derived from the video were synchronised to the MEG using nearest neighbour interpolation and appended to the dataset as supplementary trigger channels. Environmental interference was reduced by applying a Homogenous Field Correction (HFC), where the interference is modelled as a set of regular spherical harmonics derived from the sensor array (Tierney et al., 2022). Here, 8 components were projected out of the data (3 homogenous field components and 5 linear gradients). If any channels which had a residual variance larger than 100 pT (after HFC) were detected, the projection was undone, the offending channels disabled and the HFC was reapplied again without those channels included in the model. The sensor compensation matrix was also updated to account for the linear combinations of sensors in the forward modelling (Tierney et al., 2021).

2.4) Source localisation

Source localisation was performed with the DAiSS toolbox supplied with SPM12 (Litvak et al., 2011). A canonical surface representing the white matter and pial boundary was warped to fit the participant's anatomy (Mattout et al., 2007). The mesh contains 5124 vertices, which were used as the dipole locations for our source analysis. Our dipole forward model was Nolte's single shell (Nolte, 2003), where the conductive model was the boundary between the brain and CSF of the participant. Three dipoles per location representing the cardinal orientations were generated, with their degrees of freedom reduced to two to compensate for the 'silent radial source'. A linear-constrained-minimum-variance (LCMV) beamformer (Brookes et al., 2008; Van Veen et al.,

1997) was implemented to perform the inverse modelling. Here, the data covariance matrix was generated with the MEG recording band-pass-filtered into the 10-30 Hz band, which has been strongly associated with sensorimotor activity (Jurkiewicz et al., 2006; Pfurtscheller and Lopes da Silva, 1999). Due to the projection carried out during HFC in preprocessing, the MEG data are rank deficient. To control for this, the covariance matrix was regularised; the matrix decomposed into a set of eigenvectors and eigenvalues, with the 8 smallest eigenvectors/eigenvalues (associated with the 8 projected-out components from HFC) discarded (Westner et al., 2022). During LCMV, the forward models for each source were linearly combined to maximise variance from that location. (Sekihara et al., 2004).

2.5) First-level source analysis.

To map which sources in the brain covaried with the onset and offset of the behavioural states, we opted to take a 2-level general linear model (GLM) approach (Brookes et al., 2004; Quinn et al., 2022; Worsley and Friston, 1995). In particular we took an approach based on the GLM-beamfomer (Brookes et al., 2004). For the first level, we performed a mass-univariate multiple regression on each source. For each source we band-pass filtered the reconstructed source timeseries between 10-30 Hz and generated an amplitude envelope timecourse via a Hilbert transform. As power is often considered when localising motor sources, the envelopes were squared. For a given processed source signal $y \in \mathbb{R}^{n_{samples} \times 1}$, it is fitted to our general linear model,

$$y = X\beta + e,$$

where, $X \in \mathbb{R}^{n_{samples} \times n_{regressors}}$, is our design matrix with our temporal features of interest in the columns, $\beta \in \mathbb{R}^{n_{regressors} \times 1}$ are the regression coefficients, and $e \in \mathbb{R}^{n_{samples} \times 1}$ is our unexplained data. How we constructed X for each experiment differed as follows. For the motor experiment, we generated three design matrices, where the first column was either one of three features of interest. These features of interest were: the active period as specified by the block design (box car between 0-4 seconds of trial onset), a baseline 'rest' period (box car between 5-9 seconds of trial onset) or the HMM-derived active period (binarised state time-series). The second column modelled was the mean. A regression was performed for each source in the brain, generating a set of regression coefficients per vertex, which were combined to generate images. For each trial, three regression coefficient images (block active, block rest, and HMM-active) were kept for further analysis.

For the dancing experiment design, as our motor states were orthogonal in time to each other, we put in all our motor meta-states in as regressors as well as a mean and linear trend features. A single design matrix per dance was made and to generate a one regression coefficient image per meta-state, per dance. Example design matrices can be found in the supplementary material.

2.6) Second-level analysis

Motor block design

In MEG studies it is typical to contrast the movement period to a baseline (rest) epoch within the same trial (e.g. Pakenham et al., 2020). We replicate this approach in our second-level GLM. For each limb, the 1st level regression coefficient images (either block design or HMM timed) were put into a repeated-measures ANOVA design matrix with their trial-specific rest regression coefficient images and a T-contrast between the active and rest images were generated, forming a paired-T image for each limb.

Dancing

With no obvious hypothesis as to where a 'rest' period would occur in the data, we opted to contrast different movement states to each other (Ma et al., 2022). Regression coefficient images from each dance's 1st were (again) put into a repeated-measures ANOVA design matrix and T-contrasts between various limbs were generated.

3) Results

Motor block design

Figure 2 depicts the results from decoding the telemetry of the block-design experiment, were 1 of the 4 limbs were moved during a visual cue period. Figure 2A shows the binary timecourse for each condition of the experiment and the closest matching HMM state timecourse. Here the metric for matching a state to the original timecourse was the Jaccard index, with a mean±SD index for the selected 4 states of 0.65±0.06. The resultant HMM states qualitatively resemble the original experimental timeseries they were compared against. The regression heatmaps in Figure 2B show which key-points on the body were implicated in each state. We observe that the parts of the body the regression highlighted correspond to the pre-defined experimental condition.

One feature that the telemetry identifies is the reaction time between a stimulus being presented and the participant executing and concluding the movement. Figure 2C illustrates this with an example trial (where the participant was asked to moved their left arm) in which the black dashed line representing the stimulus timing, and the green solid line the corresponding HMM state. Here we can see a delay between the onset (280 ms) and offset of movement (1325 ms) compared to the initial cue. We found that across all trials the total time movement was executed for was 4.2 ± 0.9 (mean ± SD) s.

Despite the latent reaction times of the participant, we can still quantitatively compare how good the decoding of the experiment was compared to the ground truth; with the results in Figure 2D–E. Figure 2D is the confusion matrix comparing the ground truth of the experimental condition to the HMM derived Viterbi path. The Viterbi path is binarised for each labelled experimental state. Note for the 'rest' state, this represents the remaining 6 unlabelled states from the HMM. For each condition the predicted state was the most dominant, and we get an overall F_1 score (non-weighted average of the Dice coefficients; Manning et al., 2008) of 0.814. For the movement conditions we see that a proportion of the movement states are predicted to be the rest condition, which would correspond to the reaction time for the participant to initiate the movement after the cue. We also observe this effect the least for the right arm of the participant compared to the other limbs. Figure 2E shows the Receiver Operatic Characteristic (ROC) curves for the HMMs probabilistic state timeseries. Again, the timeseries for the unlabelled states are pooled together to represent the 'rest' condition. Here we are assuming are one-versus-all classification (i.e. correctly classifying a given state versus not). The areas under the curve (AUC) for each of the states are high (left leg, 0.868; right leg 0.862; left arm, 0.975; right arm, 0.990; rest, 0.8684) resulting in a macroaverage (non-weighted average) AUC 0.912. We also performed a split-half cross-validation, which showed similar levels of performance (see supplementary material).

Figure 3 shows the T-contrasts between the rest period and either the original experimental-derived active epochs or the HMM-derived epochs for each of the 4 experimental conditions. The functional images have been overlaid on inflated cortical surfaces, where gyri are in light grey and the sulci in dark grey. For clarity we have applied a threshold of 70% of the most extreme T-statistic in the image. In all conditions we observe the characteristic event related desynchronisation (ERD) of beta-band power during movement. For each image a magenta dot represents the location of the peak T-statistic when contrasting movement and rest. Focusing on the block-design derived results (left panel of Figure 3), we first observe that the all the peak locations are in the precentral gyrus (motor cortex) rather than the postcentral (somatosensory cortex). Second, we see that all 4 of the images follow the traditional organisation of the motor cortex (Gordon et al., 2023; Penfield and Boldrey, 1937), with the arm condition peaks localised more dorsal, and the leg peaks appearing medially. Considering the results of the HMM-derived timings we note two things. First, the peak locations are very close between the two approaches (peak T-statistics in identical vertices between the two approaches). Second, the threshold statistical maps are similar in their morphology and their T-statistics are of a similar magnitude to the block design images.

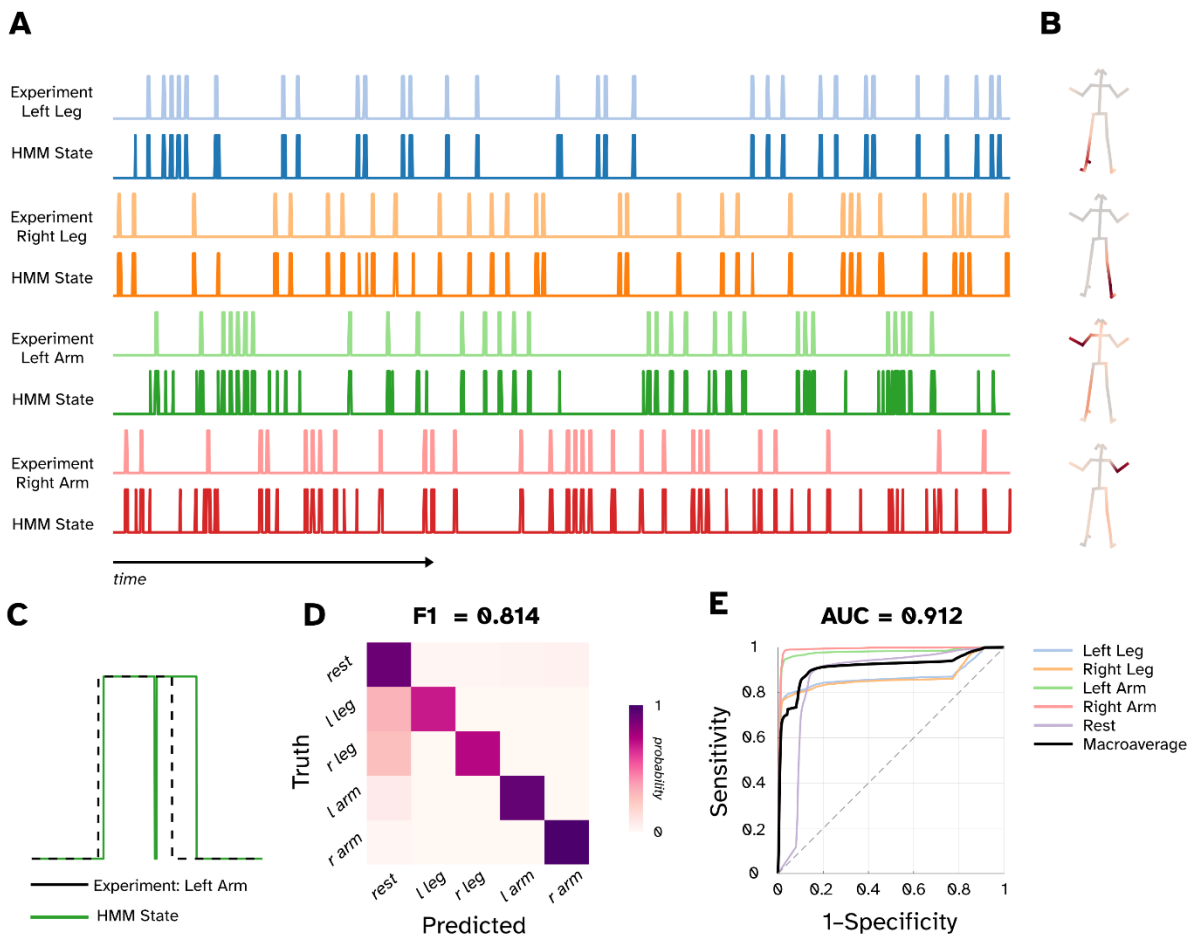

Figure 2 – A comparison of the HMM-derived video telemetry states in comparison to the original experiment design for a simple 4 condition motor task. ***A)*** *Temporal plots depicting the 4 experimentally derived states across a recording represented as binary signals. Plotted below each experimental timecourse is the corresponding telemetry state which closest matched each experimental condition. The duration of each movement was 4.2 ± 0.9 (mean ± SD) s.* ***B)*** *Heatmaps corresponding to the regression of the HMM state timecourse against the original telemetry data to identify which body parts were moving in a given state; the darker the plot, the stronger the relationship between telemetry data and a given HMM state.* ***C)*** *A portion of the left arm experimental state (black dashed line) and the closest matched HMM state (green solid line) which demonstrates the delay (280 ms onset, 1325 ms offset) between presentation of experimental cue and execution/cessation of movement.* ***D)*** *Multi-class confusion matrices showing the probability of a given HMM state being active compared to the experimental ground truth.* ***E)*** *Receiver operating characteristic (ROC) curves for the resultant HMM compared to the block design it is predicting. Pale colours represent the states representing specific conditions in a (one v. all) classification, black line represents the macroaverage (unweighted mean) of all 5 ROC curves.*

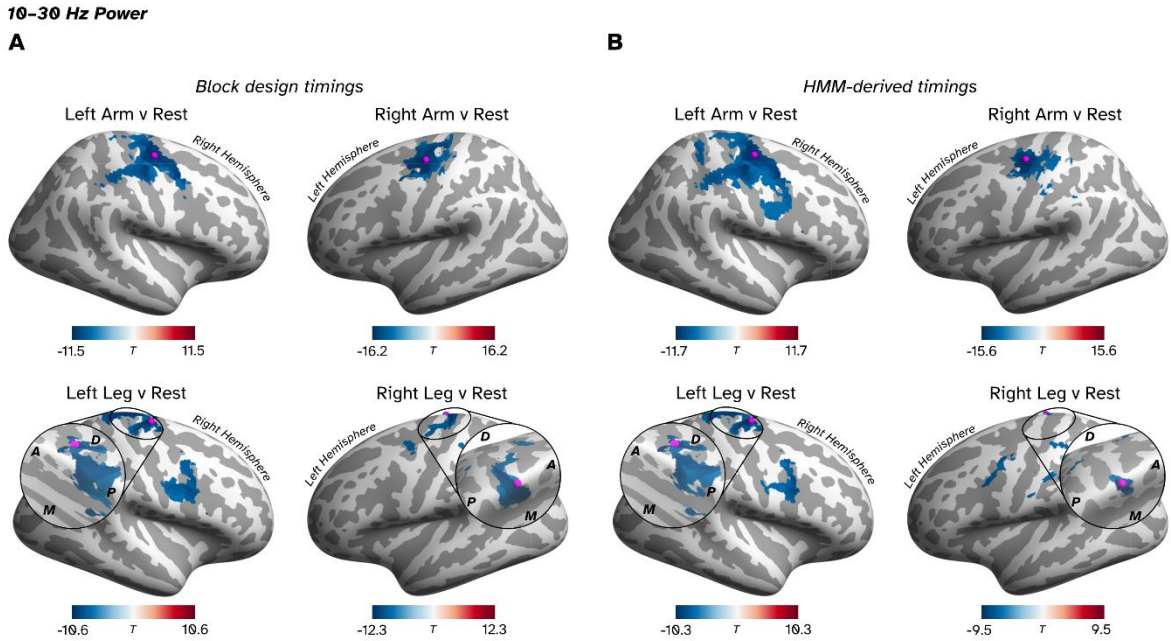

Figure 3 – Source localisation results of a block designed, 4-condition motor experiment in a single subject, with results presented on an inflated cortical surface. Dark grey areas represent the sulci in the brain and light grey the gyri. ***A)*** *T-contrasts for the 4 active conditions v. rest based on the timings specified by the block design.* ***B)*** *T-contrasts for the 4 active conditions v. rest based on the HMM-derived timings. Magenta spheres represent the global peaks of each image. Images representing the Leg v Rest conditions also have a sub-plot showing a zoomed and rotated representation of the medial areas of the brain to highlight activity originating from the leg/ foot areas of the motor cortex. Images have been threshold to show anything within 70% of the most extreme statistic.*

Dancing

Having established that our video telemetry pipeline works with a traditional motor paradigm, we extended our investigation to a series of more complex movements during a choreographed dance routine. Of the 25 states extracted from the telemetry, 13 were categorised into 5 meta-states, based on which key points on the body were employed. These meta-states were used to epoch the MEG data for further analyses. The heatmaps of these meta-states are depicted in Figure 4A. These represented each of the 4 individual limbs and a state representing both arms being moved in unison. Individual maps and timeseries of the 25 states can be found in the supplementary material. Figure 4B shows the fractional occupancy of a meta-state across the 15 sessions, which reveals a clear temporal structure emerging from the dance across all subjects and sessions. We see that each of the individual limb states dominate for a verse and chorus and crucially the dominant state corresponds to the theme of the verse (*"You put your left arm in"* for verse 1, right arm for verse 2 etc). We can also observe when a participant switches from one limb to another even within a verse. For example, at the 16 second mark where people transition from moving one arm to both at the line *"you do the hokey-cokey"* the dominant state switches from the left arm state (blue line) to the both arms state (purple line).

Activation maps, as defined by contrasting different movement states, are depicted in Figure 5. In particular we focus on three main contrasts of interest, with additional exploratory contrasts in the supplementary material. For clarity we have masked these images to only show activations from the pre- and post-central gyri, but the unmasked (and unthreshold) images of these states can also be found in the supplementary information. For Figures 5A and 5B, we generated paired-T contrasts, where both arms moving (purple state in Figure 4B) were subtracted from one of the single arm states. First, we contrast *both arms* to *left arm* movement (Fig. 5A; [-1 1] contrast) and the resultant paired-T image shows activation over the left dorsal sensorimotor areas (associated with right-upper limb movement). To get an activation of the right arm may be counterintuitive, but we note that contrasting both arms to a single arm should result in the activation map of the un-contrasted limb from a set theory perspective (the contrast represents the disjunctive union of the two limbs). Further supporting this idea is the opposite contrast of *both arms* to *right arm* (Fig. 5B; [-1 1] contrast), where we see a significant interaction in the opposite hemisphere, representing left-arm movement. We note that we attempted to contrast single arm movements against each other (i.e. left arm – right arm). Whilst this did give the expected anti-symmetric

distribution of T-values (positive one hemisphere, negative the other), the magnitude of the T-values was heavily lateralised. (see supplementary material). Using a both arms versus one arm approach appears to control for this "imbalance". Finally, we attempted to localise the legs. Initially, we tried to contrast one leg against the other but the resulting images did not fit with expectation of largest T-values over the medial motor cortex (see supplementary information), with the lower T-values over the medial motor cortex than elsewhere, implying that power in these postulated leg areas overlapped. When we summed the *left leg* and *right leg* states (Fig 5C; [1 1] contrast) to make a pooled 1-sample T-image, we found that what activation was seen in the sensorimotor areas was localised to the medial areas of the brain corresponding to lower limb movement. Here the contrast represents where the union of the two states deviates away from the mean amplitude across the entire experiment, which lends evidence to our hypothesis that these areas may be co-activated in standing leg movement.

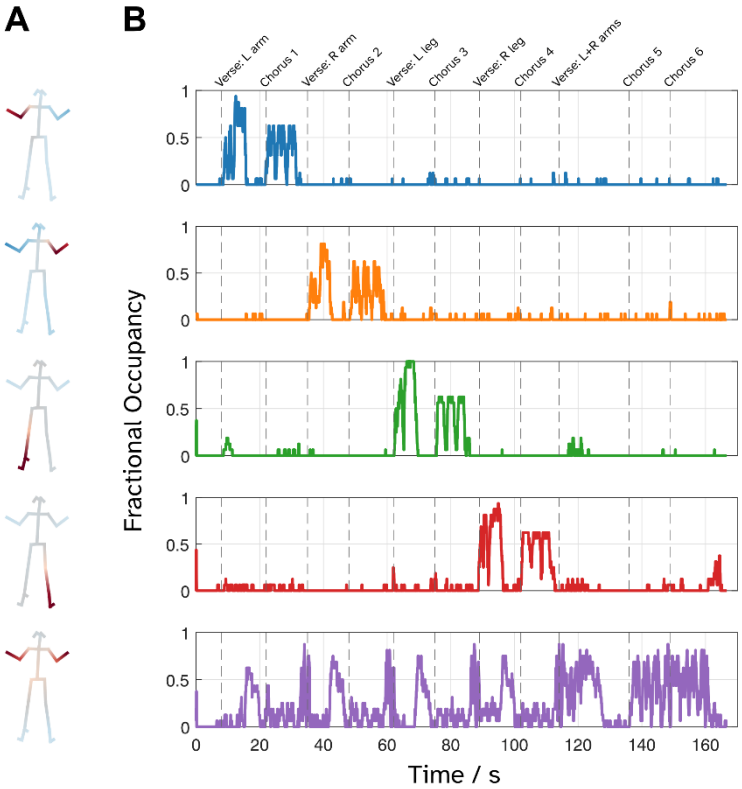

Figure 4 – Five telemetry states extracted from the video of the 4 participants dancing to the Hokey Cokey. ***A)*** *The heatmaps related to regressing the binarised state timecourses against the key-point velocity data, deep red areas show the parts of the body represented the most by each state.* ***B)*** *Session-averaged timecourses for each state, generating fractional occupancy timeseries, revealing the onset and offsets of dominant states over the progression of the dance.*

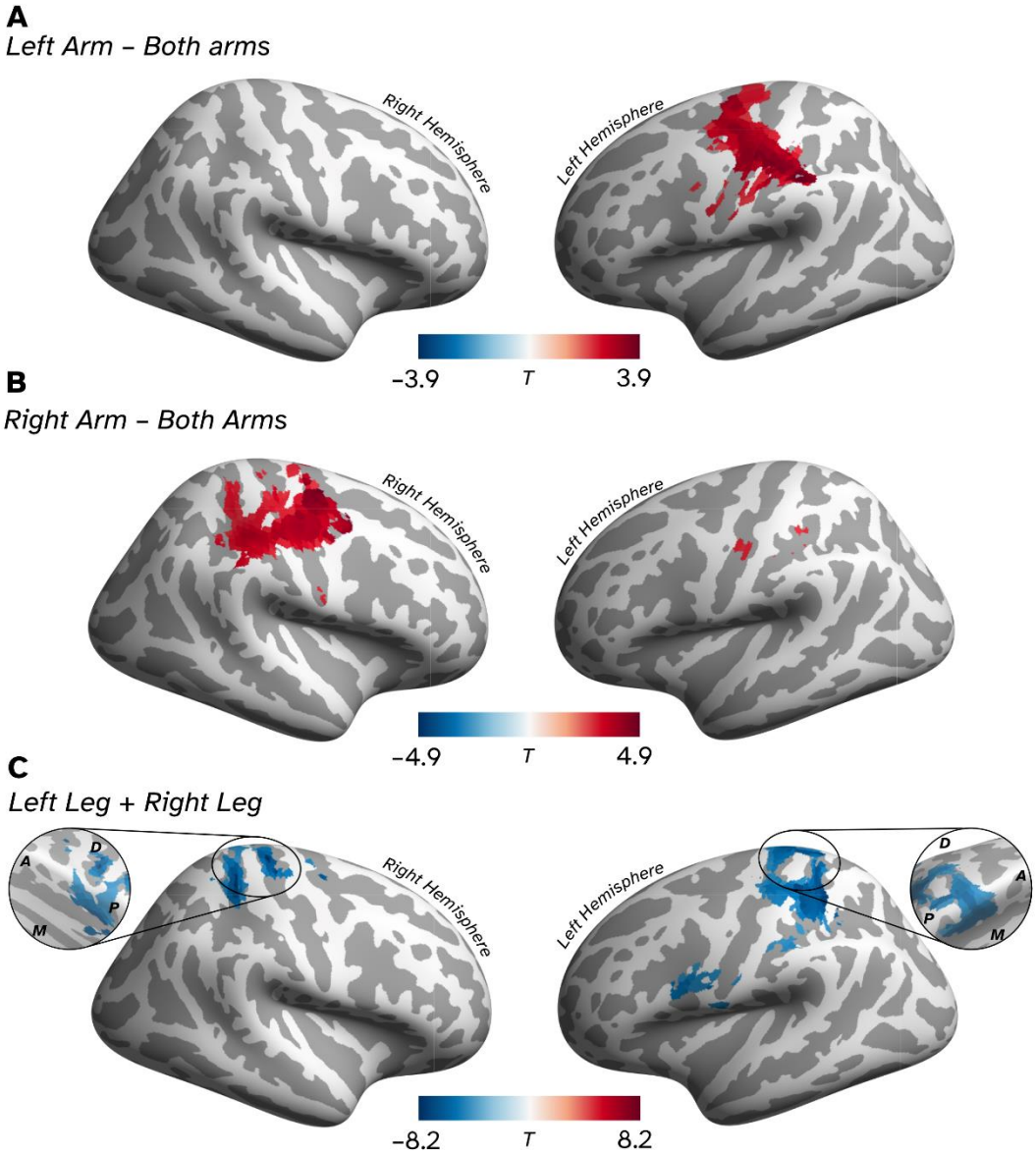

Figure 5 – Group activation effects of 10-30 Hz power contrasted between different motor states, shown on inflated cortical surfaces. ***A)*** *Contrasting power from both arms moving to just the left arm ([-1 1] contrast) results in an activation map of the right arm.* ***B)*** *Contrasting both arms to the right arm ([-1 1] contrast), and therefore a left arm's activation remains.* ***C)*** *Summing the left and right leg states ([1 1] contrast) reveals largest activations over the medial motor areas. For all images the threshold was set to 50% of the most extreme T-value.*

5) Discussion

Wearable MEG systems (such as those using OPMs) are key technologies for the future of naturalistic, mobile neuroimaging (Stangl et al., 2023). Work on making wearable MEG systems compatible with immersive virtual environments (Roberts et al., 2019) and ambulatory movement (Holmes et al., 2023b; Mellor et al., 2023; Seymour et al., 2021a) is already well underway. However, the collection, analysis and fusion of complex behavioural data during the experiment with MEG data is something which studies will need to address. Here we have introduced a processing framework of movement data to demonstrate how this could be approached.

We have shown that it is possible to provide crucial experimental timings to process OP-MEG data, entirely from markerless decomposition of behavioural data, derived with open-source machine learning approaches applied to videos of participants executing limb movements. With this approach, we could not only decode the experimental condition from a block design, but using these derived timings could also replicate the activation maps derived from the traditional-block design timings. We then applied this approach to a dancing paradigm, where after some basic choreography instruction to the participants, all movement execution was voluntary. From these video recordings, we derived neuronal states associated with dance moves, which organized as distinct representations of the limbs along the sensorimotor cortical surface. Our approach is particularly powerful for naturalistic studies, where precise, regular timings across participants are not guaranteed. Had we set experimental timings to the lyrical cues played to the participants, it would have overlooked the variability in subjects' actual moves during the dance. By decoding these motor states within the behavioural data, we recover the subject-specific timings and factor in what could be previously described as 'noise' in our experimental design. This had been identified as one of the key challenges to developing successful mobile, naturalistic neuroimaging studies (Stangl et al., 2023).

Using regular (optical) video data to analyse movement with neural-network-based pose estimators (Bazarevsky et al., 2020; Cao et al., 2021; Mathis et al., 2018) can forgo the need of additional infra-red retro-reflective markers on the body. This has the additional benefit for the family of OPMs we use, which use infra-red laser light to operate (and can be subject to interference from other light sources). The use of Hidden Markov Models (HMMs) to partition motion telemetry data is not uncommon (Agrahri et al., 2022; Buderman et al., 2021; Conners et al., 2021; Singh et al., 2021), as they are able to exploit the temporally-rich nature of the multivariate motion data. We also note that HMMs are also very popular in neuroimaging analysis and we in fact used a HMM toolbox primarily designed to accommodate neuroimaging data (Vidaurre et al., 2016). Future work could look at the synergy of the states derived from the motor telemetry and MEG data to find commonality between the two disparate measures.

In our data, we were pleased that our results clustered into locations of the upper limb movements (dorsal motor cortex) and lower limb areas (medial motor cortex) that conform with the functional neuroanatomy of the sensorimotor cortices (Gordon et al., 2023; Jensen et al., 2022; Penfield and Boldrey, 1937). This separation was clear in the block-design motor experiment, where the participant was seated and it was easier to move a limb in isolation. For the dancing paradigm, we were initially surprised that the observed functional maps (particularly lower limb) did not better correspond with the predicted motor/somatotopy without pooling the images together. It is noteworthy, however, that the subjects were moving their whole bodies during each dance move. For example, it is almost impossible to lift ones left leg without moving other limbs and torso to rebalance. This also (in part) explains why there was activation within these lower limb areas only when contrasting the leg states together rather than subtracting from each other, as both legs would have been employed even when only one leg showed major movement. This type of motor paradigm is in contrast to previous experiments, either during surgery (Penfield and Boldrey, 1937) or with subjects immobile in a scanner, in which only a single body part is moved or stimulated (Barratt et al., 2018; Huber et al., 2020; Krishnamurthy et al., 2022; Ma et al., 2022; Nakamura et al., 1998). In other words, here the data might better represent changes in posture rather than changes in individual body parts. One might argue, moving forward to more natural paradigms, posture mapping may be of more clinical and neuroscientific interest, as it better reflects movements made in daily life. This investigation provides a proof-of-principle of the potential of wearable MEG to facilitate functional neuroimaging without a highly controlled behavioural tasks.

As well as impacting naturalistic neuroscience research, this could be used in the clinic. Assessing pose-based behavioural data has been shown beneficial in assessing Parkinson's disease (Roth et al., 2021; Sabo et al., 2022), the progress of Friedreich's ataxia (Kadirvelu et al., 2023), as well as detecting non-verbal behaviour in Autistic Spectrum Disorder (Kojovic et al., 2021). Furthermore, combining these methods with a flexible

neuroimaging system such as OP-MEG promises to improve our understanding of these conditions in ways previously unavailable to us. There are direct clinical pathways where this could immediately benefit, such as in paediatric cases. For example, cases of refectory (drug resistant) epilepsy where surgical intervention is required often carefully localise eloquent cortex with functional neuroimaging – to ensure that key faculties are not interfered with when removing the seizure onset zone. This is typically assessed with functional MRI (Al-Arfaj et al., 2023; Barras et al., 2016), but success of the mapping is limited to the performance of the patient, and their tolerance of the MR system. For young children with epilepsy, this effect may be compounded (Yerys et al., 2009). Solutions to this might include trying to map the motor areas in the resting state (Krishnamurthy et al., 2022), but we believe there is a more naturalistic alternative. Children playing when undergoing video-M/EEG telemetry sessions for seizure monitoring will enter states of movement and periods of rest naturally. If the video footage was processed to demarcate these periods it is entirely feasible that these motor maps (and indeed language or other key regions of eloquent cortex) may be able to be derived *for free* out of long recordings where the primary goal is to locate ictal/interictal activity. This idea using play in neuroimaging may also be favourable other conditions too, such investigating the progress of motor development in children with Autistic Spectrum Disorder (An et al., 2021; Wilson et al., 2018), where a flexible imaging system which can adapt to the child, whilst simultaneously tracking movement should to more successful recording sessions than a large unadaptable system.

One technical aspect about the OP-MEG acquisition is the lack of additional active shielding applied to our OPM recordings. Our magnetic shielded room provides adequate shielding in the centre of the room to provide a low enough field to keep the sensors in their operational range (up to 4.5 nT from their initialisation point). However, we did not account for cross-axis projection errors (CAPE; Borna et al., 2022), which become apparent in recordings when the background field deviates by approximately 1 nT or more from the sensor's zero point. Cross-axis projection errors result in additional asymmetrical non-linearities in the field-to-voltage response of the sensors (Schofield et al., 2023), which in turn has an impact on source localisation performance (Borna et al., 2022). In our block-designed motor experiment, the largest field experiences by any sensor was 2.1 nT from its zero-point. For the dancing data, the largest fields measured for each of the 4 subjects were 1.5 nT, 0.6 nT, 1.2 nT and 3.5 nT from their zero-point. It is clear that the data presented here would contain CAPE effects, but given the activation maps presented here, we do not think this invalidates our findings. Methods which counteract field changes experiences by the sensors during ambulatory motion, whether through dedicated nulling coils built into the shielded room (Holmes et al., 2023b) or by using a dynamic closed-loop system built directly into the sensors (Lee et al., 2014; Mellor et al., 2023; Nardelli et al., 2019; Robinson et al., 2022) should be employed for future studies to control for CAPE-related nonlinearities.

To conclude, our work provides additional support for the exciting opportunity of OP-MEG for studying the neural basis of complex motor functions, but also spatial navigation, memory and social interactions in realistic and ecologically valid situations, in health and disease.

6) Acknowledgements

Funding for this project was provided by EPSRC (EP/T001046/1) from the Quantum Technology hub in sensing and timing (sub-award QTPRF02) awarded to GRB and MJB. SM is funded by EPSRC-HIP award (EP/V047264/1). NAA, RAS are supported by a Wellcome Principal Research Fellowship (210567/Z/18/Z). TMT is funded by a fellowship from Epilepsy Research UK and Young Epilepsy (FY2101). MFH is supported by a Non-Clinical Post Doctorial Fellowship from the Guarantors of Brain. MS is supported by a Wellcome Technology development award (223736/Z/21/Z). The Wellcome Centre for Human Neuroimaging is supported by core funding from Wellcome (203147/Z/16/Z). The GPU was supported by an NVIDIA academic hardware grant awarded to MFH.

7) Conflict of interest declaration

MJB is a director of Cerca Magnetics Limited, a spin-out company whose aim is to commercialise aspects of OP-MEG technology MJB also holds founding equity in Cerca Magnetics Limited.

8) Data and code availability

The MATLAB scripts used to analyse the data are available at https://github.com/georgeoneill/videomeg. Openpose 1.7.0 is available to download from https://github.com/CMU-Perceptual-Computing-Lab/openpose. The data, downsampled to 2 kHz (with antialiasing applied) is available to download from Zenodo at

https://doi.org/10.5281/zenodo.8139849. Openpose telemetry data from the video is included. To conform with data protection regulations, we cannot share the original video on which the pose inference was performed.

References

Agrahri, A., Tyagi, A., Kumar, D., Kusumakar, S., Palaniswami, M., Yan, B., 2022. Detection of Epileptic Seizure Using Accelerometer Time Series Data and Hidden Markov Model, in: 2022 44th Annual International Conference of the IEEE Engineering in Medicine & Biology Society (EMBC). Presented at the 2022 44th Annual International Conference of the IEEE Engineering in Medicine & Biology Society (EMBC), pp. 2426–2429. https://doi.org/10.1109/EMBC48229.2022.9871914

Al-Arfaj, H.K., Al-Sharydah, A.M., AlSuhaibani, S.S., Alaqeel, S., Yousry, T., 2023. Task-Based and Resting-State Functional MRI in Observing Eloquent Cerebral Areas Personalized for Epilepsy and Surgical Oncology Patients: A Review of the Current Evidence. Journal of Personalized Medicine 13, 370. https://doi.org/10.3390/jpm13020370

Altarev, I., Fierlinger, P., Lins, T., Marino, M.G., Nießen, B., Petzoldt, G., Reisner, M., Stuiber, S., Sturm, M., Taggart Singh, J., Taubenheim, B., Rohrer, H.K., Schläpfer, U., 2015. Minimizing magnetic fields for precision experiments. Journal of Applied Physics 117, 233903. https://doi.org/10.1063/1.4922671

An, K., Ikeda, T., Hasegawa, C., Yoshimura, Y., Tanaka, S., Saito, D.N., Yaoi, K., Iwasaki, S., Hirosawa, T., Jensen, O., Kikuchi, M., 2021. Aberrant brain oscillatory coupling from the primary motor cortex in children with autism spectrum disorders. NeuroImage: Clinical 29, 102560. https://doi.org/10.1016/j.nicl.2021.102560

Anderson, D.J., Perona, P., 2014. Toward a Science of Computational Ethology. Neuron 84, 18–31. https://doi.org/10.1016/j.neuron.2014.09.005

Barras, C.D., Asadi, H., Baldeweg, T., Manchini, L., Yousry, T., Bisdas, S., 2016. Functional magnetic resonance imaging in clinical practice: State of the art and science. Australian Journal for General Practitioners 45, 798–803.

Barratt, E.L., Francis, S.T., Morris, P.G., Brookes, M.J., 2018. Mapping the topological organisation of beta oscillations in motor cortex using MEG. NeuroImage. https://doi.org/10.1016/j.neuroimage.2018.06.041

Barry, D.N., Tierney, T.M., Holmes, N., Boto, E., Roberts, G., Leggett, J., Bowtell, R., Brookes, M.J., Barnes, G.R., Maguire, E.A., 2019. Imaging the human hippocampus with optically-pumped magnetoencephalography. NeuroImage 203, 116192. https://doi.org/10.1016/j.neuroimage.2019.116192

Bazarevsky, V., Grishchenko, I., Raveendran, K., Zhu, T., Zhang, F., Grundmann, M., 2020. BlazePose: On-device Real-time Body Pose tracking. https://doi.org/10.48550/arXiv.2006.10204

Betti, V., Della Penna, S., de Pasquale, F., Mantini, D., Marzetti, L., Romani, G.L., Corbetta, M., 2013. Natural Scenes Viewing Alters the Dynamics of Functional Connectivity in the Human Brain. Neuron 79, 782–797. https://doi.org/10.1016/j.neuron.2013.06.022

Black Lace, 1985. Hokey Cokey. Flair Records.

Borna, A., Carter, T.R., Goldberg, J.D., Colombo, A.P., Jau, Y.-Y., Berry, C., McKay, J., Stephen, J., Weisend, M., Schwindt, P.D.D., 2017. A 20-channel magnetoencephalography system based on optically pumped magnetometers. Phys. Med. Biol. 62, 8909–8923. https://doi.org/10.1088/1361-6560/aa93d1

Borna, A., Iivanainen, J., Carter, T.R., McKay, J., Taulu, S., Stephen, J., Schwindt, P.D.D., 2022. Cross-Axis projection error in optically pumped magnetometers and its implication for magnetoencephalography systems. NeuroImage 247, 118818. https://doi.org/10.1016/j.neuroimage.2021.118818

Boto, E., Holmes, N., Leggett, J., Roberts, G., Shah, V., Meyer, S.S., Muñoz, L.D., Mullinger, K.J., Tierney, T.M., Bestmann, S., Barnes, G.R., Bowtell, R., Brookes, M.J., 2018. Moving magnetoencephalography towards real-world applications with a wearable system. Nature 555, 657–661. https://doi.org/10.1038/nature26147

Boto, E., Meyer, S.S., Shah, V., Alem, O., Knappe, S., Kruger, P., Fromhold, T.M., Lim, M., Glover, P.M., Morris, P.G., Bowtell, R., Barnes, G.R., Brookes, M.J., 2017. A new generation of magnetoencephalography: Room temperature measurements using optically-pumped magnetometers. NeuroImage 149, 404–414. https://doi.org/10.1016/j.neuroimage.2017.01.034

Boto, E., Seedat, Z.A., Holmes, N., Leggett, J., Hill, R.M., Roberts, G., Shah, V., Fromhold, T.M., Mullinger, K.J., Tierney, T.M., Barnes, G.R., Bowtell, R., Brookes, M.J., 2019. Wearable neuroimaging: Combining and contrasting magnetoencephalography and electroencephalography. NeuroImage 201, 116099. https://doi.org/10.1016/j.neuroimage.2019.116099

Brookes, M.J., Gibson, A.M., Hall, S.D., Furlong, P.L., Barnes, G.R., Hillebrand, A., Singh, K.D., Holliday,

I.E., Francis, S.T., Morris, P.G., 2004. A general linear model for MEG beamformer imaging. NeuroImage 23, 936–946. https://doi.org/10.1016/j.neuroimage.2004.06.031

Brookes, M.J., Vrba, J., Robinson, S.E., Stevenson, C.M., Peters, A.M., Barnes, G.R., Hillebrand, A., Morris, P.G., 2008. Optimising experimental design for MEG beamformer imaging. Neuroimage 39, 1788–1802.

Buderman, F.E., Gingery, T.M., Diefenbach, D.R., Gigliotti, L.C., Begley-Miller, D., McDill, M.M., Wallingford, B.D., Rosenberry, C.S., Drohan, P.J., 2021. Caution is warranted when using animal space-use and movement to infer behavioral states. Movement Ecology 9, 30. https://doi.org/10.1186/s40462-021-00264-8

Cao, Z., Hidalgo, G., Simon, T., Wei, S.-E., Sheikh, Y., 2021. OpenPose: Realtime Multi-Person 2D Pose Estimation Using Part Affinity Fields. IEEE Transactions on Pattern Analysis and Machine Intelligence 43, 172–186. https://doi.org/10.1109/TPAMI.2019.2929257

Cohen, D., 1972. Magnetoencephalography: detection of the brain's electrical activity with a superconducting magnetometer. Science 175, 664–666.

Conners, M.G., Michelot, T., Heywood, E.I., Orben, R.A., Phillips, R.A., Vyssotski, A.L., Shaffer, S.A., Thorne, L.H., 2021. Hidden Markov models identify major movement modes in accelerometer and magnetometer data from four albatross species. Movement Ecology 9, 7. https://doi.org/10.1186/s40462-021-00243-z

de Lange, P., Boto, E., Holmes, N., Hill, R.M., Bowtell, R., Wens, V., De Tiège, X., Brookes, M.J., Bourguignon, M., 2021. Measuring the cortical tracking of speech with optically-pumped magnetometers. NeuroImage 233, 117969. https://doi.org/10.1016/j.neuroimage.2021.117969

Feys, O., Corvilain, P., Aeby, A., Sculier, C., Holmes, N., Brookes, M., Goldman, S., Wens, V., De Tiège, X., 2022. On-Scalp Optically Pumped Magnetometers versus Cryogenic Magnetoencephalography for Diagnostic Evaluation of Epilepsy in School-aged Children. Radiology 304, 429–434. https://doi.org/10.1148/radiol.212453

Feys, O., Corvilain, P., Van Hecke, A., Sculier, C., Rikir, E., Legros, B., Gaspard, N., Leurquin-Sterk, G., Holmes, N., Brookes, M., Goldman, S., Wens, V., De Tiège, X., 2023. Recording of Ictal Epileptic Activity Using on-Scalp Magnetoencephalography. Annals of Neurology 93, 419–421. https://doi.org/10.1002/ana.26562

Finn, E.S., Glerean, E., Hasson, U., Vanderwal, T., 2022. Naturalistic imaging: The use of ecologically valid conditions to study brain function. NeuroImage 247, 118776. https://doi.org/10.1016/j.neuroimage.2021.118776

Gordon, E.M., Chauvin, R.J., Van, A.N., Rajesh, A., Nielsen, A., Newbold, D.J., Lynch, C.J., Seider, N.A., Krimmel, S.R., Scheidter, K.M., Monk, J., Miller, R.L., Metoki, A., Montez, D.F., Zheng, A., Elbau, I., Madison, T., Nishino, T., Myers, M.J., Kaplan, S., Badke D'Andrea, C., Demeter, D.V., Feigelis, M., Ramirez, J.S.B., Xu, T., Barch, D.M., Smyser, C.D., Rogers, C.E., Zimmermann, J., Botteron, K.N., Pruett, J.R., Willie, J.T., Brunner, P., Shimony, J.S., Kay, B.P., Marek, S., Norris, S.A., Gratton, C., Sylvester, C.M., Power, J.D., Liston, C., Greene, D.J., Roland, J.L., Petersen, S.E., Raichle, M.E., Laumann, T.O., Fair, D.A., Dosenbach, N.U.F., 2023. A somato-cognitive action network alternates with effector regions in motor cortex. Nature 1–9. https://doi.org/10.1038/s41586-023-05964-2

Hämäläinen, M., Hari, R., Ilmoniemi, R.J., Knuutila, J., Lounasmaa, O.V., 1993. Magnetoencephalography theory, instrumentation, and applications to noninvasive studies of the working human brain. Reviews of Modern Physics 65, 413–497. https://doi.org/10.1103/RevModPhys.65.413

Hill, R.M., Boto, E., Holmes, N., Hartley, C., Seedat, Z.A., Leggett, J., Roberts, G., Shah, V., Tierney, T.M., Woolrich, M.W., Stagg, C.J., Barnes, G.R., Bowtell, R., Slater, R., Brookes, M.J., 2019. A tool for functional brain imaging with lifespan compliance. Nat Commun 10, 4785. https://doi.org/10.1038/s41467-019-12486-x

Hill, R.M., Boto, E., Rea, M., Holmes, N., Leggett, J., Coles, L.A., Papastavrou, M., Everton, S.K., Hunt, B.A.E., Sims, D., Osborne, J., Shah, V., Bowtell, R., Brookes, M.J., 2020. Multi-channel whole-head OPM-MEG: Helmet design and a comparison with a conventional system. NeuroImage 219, 116995. https://doi.org/10.1016/j.neuroimage.2020.116995

Hillebrand, A., Holmes, N., Sijsma, N., O'Neill, G.C., Tierney, T.M., Liberton, N., Stam, A.H., van Klink, N., Stam, C.J., Bowtell, R., Brookes, M.J., Barnes, G.R., 2023. Non-invasive measurements of ictal and interictal epileptiform activity using optically pumped magnetometers. Sci Rep 13, 4623. https://doi.org/10.1038/s41598-023-31111-y

Holmes, N., Rea, M., Hill, R.M., Boto, E., Leggett, J., Edwards, L.J., Rhodes, N., Shah, V., Osborne, J., Fromhold, T.M., Glover, P., Montague, P.R., Brookes, M.J., Bowtell, R., 2023a. Naturalistic Hyperscanning with Wearable Magnetoencephalography. Sensors 23, 5454. https://doi.org/10.3390/s23125454

Holmes, N., Rea, M., Hill, R.M., Leggett, J., Edwards, L.J., Hobson, P.J., Boto, E., Tierney, T.M., Rier, L.,

Rivero, G.R., Shah, V., Osborne, J., Fromhold, T.M., Glover, P., Brookes, M.J., Bowtell, R., 2023b. Enabling ambulatory movement in wearable magnetoencephalography with matrix coil active magnetic shielding. NeuroImage 274, 120157. https://doi.org/10.1016/j.neuroimage.2023.120157

Huber, L., Finn, E.S., Handwerker, D.A., Bönstrup, M., Glen, D.R., Kashyap, S., Ivanov, D., Petridou, N., Marrett, S., Goense, J., Poser, B.A., Bandettini, P.A., 2020. Sub-millimeter fMRI reveals multiple topographical digit representations that form action maps in human motor cortex. NeuroImage 208, 116463. https://doi.org/10.1016/j.neuroimage.2019.116463

Iivanainen, J., Zetter, R., Grön, M., Hakkarainen, K., Parkkonen, L., 2019. On-scalp MEG system utilizing an actively shielded array of optically-pumped magnetometers. NeuroImage 194, 244–258. https://doi.org/10.1016/j.neuroimage.2019.03.022

Jaccard, P., 1912. The Distribution of the Flora in the Alpine Zone. New Phytologist 11, 37–50. https://doi.org/10.1111/j.1469-8137.1912.tb05611.x

Jensen, M.A., Huang, H., Valencia, G.O., Klassen, B.T., Boom, M.A. van den, Kaufmann, T.J., Schalk, G., Brunner, P., Hermes, D., Worrell, G.A., Miller, K.J., 2022. Homunculus Interruptus: A motor association area in the depth of the central sulcus. https://doi.org/10.1101/2022.11.20.517292

Jurkiewicz, M.T., Gaetz, W.C., Bostan, A.C., Cheyne, D., 2006. Post-movement beta rebound is generated in motor cortex: Evidence from neuromagnetic recordings. NeuroImage 32, 1281–1289. https://doi.org/10.1016/j.neuroimage.2006.06.005

Kadirvelu, B., Gavriel, C., Nageshwaran, S., Chan, J.P.K., Nethisinghe, S., Athanasopoulos, S., Ricotti, V., Voit, T., Giunti, P., Festenstein, R., Faisal, A.A., 2023. A wearable motion capture suit and machine learning predict disease progression in Friedreich's ataxia. Nat Med 29, 86–94. https://doi.org/10.1038/s41591-022-02159-6

Kim, D., Kay, K., Shulman, G.L., Corbetta, M., 2018. A New Modular Brain Organization of the BOLD Signal during Natural Vision. Cerebral Cortex 28, 3065–3081. https://doi.org/10.1093/cercor/bhx175

Knappe, S., Alem, O., Sheng, D., Kitching, J., 2016. Microfabricated Optically-Pumped Magnetometers for Biomagnetic Applications. J. Phys.: Conf. Ser. 723, 012055. https://doi.org/10.1088/1742-6596/723/1/012055

Kojovic, N., Natraj, S., Mohanty, S.P., Maillart, T., Schaer, M., 2021. Using 2D video-based pose estimation for automated prediction of autism spectrum disorders in young children. Sci Rep 11, 15069. https://doi.org/10.1038/s41598-021-94378-z

Kringelbach, M.L., Perl, Y.S., Tagliazucchi, E., Deco, G., 2023. Toward naturalistic neuroscience: Mechanisms underlying the flattening of brain hierarchy in movie-watching compared to rest and task. Science Advances 9, eade6049. https://doi.org/10.1126/sciadv.ade6049

Krishnamurthy, M., You, X., Sepeta, L.N., Matuska, E., Oluigbo, C., Berl, M.M., Gaillard, W.D., Gholipour, T., 2022. Resting-state functional MRI for motor cortex mapping in childhood-onset focal epilepsy. Journal of Neuroimaging 32, 1201–1210. https://doi.org/10.1111/jon.13030

Lee, H.J., Shim, J.H., Moon, H.S., Kim, K., 2014. Flat-response spin-exchange relaxation free atomic magnetometer under negative feedback. Opt. Express, OE 22, 19887–19894. https://doi.org/10.1364/OE.22.019887

Litvak, V., Mattout, J., Kiebel, S., Phillips, C., Henson, R., Kilner, J., Barnes, G., Oostenveld, R., Daunizeau, J., Flandin, G., Penny, W., Friston, K., 2011. EEG and MEG Data Analysis in SPM8. Computational Intelligence and Neuroscience 2011, e852961. https://doi.org/10.1155/2011/852961

Ma, S., Huang, T., Qu, Y., Chen, X., Zhang, Y., Zhen, Z., 2022. An fMRI dataset for whole-body somatotopic mapping in humans. Sci Data 9, 515. https://doi.org/10.1038/s41597-022-01644-4

Manning, C.D., Raghavan, P., Schütze, H., 2008. Introduction to Information Retrieval. Cambridge University Press.

Mathis, A., Mamidanna, P., Cury, K.M., Abe, T., Murthy, V.N., Mathis, M.W., Bethge, M., 2018. DeepLabCut: markerless pose estimation of user-defined body parts with deep learning. Nat Neurosci 21, 1281–1289. https://doi.org/10.1038/s41593-018-0209-y

Mattout, J., Henson, R.N., Friston, K.J., 2007. Canonical Source Reconstruction for MEG. Computational Intelligence and Neuroscience 2007, e67613. https://doi.org/10.1155/2007/67613

Mellor, S., Tierney, T.M., Seymour, R.A., Timms, R.C., O'Neill, G.C., Alexander, N., Spedden, M.E., Payne, H., Barnes, G.R., 2023. Real-time, model-based magnetic field correction for moving, wearable MEG. NeuroImage 120252. https://doi.org/10.1016/j.neuroimage.2023.120252

Meyer, S.S., Bonaiuto, J., Lim, M., Rossiter, H., Waters, S., Bradbury, D., Bestmann, S., Brookes, M., Callaghan, M.F., Weiskopf, N., Barnes, G.R., 2017. Flexible head-casts for high spatial precision {MEG}. Journal of Neuroscience Methods 276, 38–45. https://doi.org/10.1016/j.jneumeth.2016.11.009

Muthukumaraswamy, S., 2013. High-frequency brain activity and muscle artifacts in MEG/EEG: A review and recommendations. Frontiers in Human Neuroscience 7.

Nakamura, A., Yamada, T., Goto, A., Kato, T., Ito, K., Abe, Y., Kachi, T., Kakigi, R., 1998. Somatosensory

Homunculus as Drawn by MEG. NeuroImage 7, 377–386. https://doi.org/10.1006/nimg.1998.0332
Nardelli, N.V., Krzyzewski, S.P., Knappe, S.A., 2019. Reducing crosstalk in optically-pumped magnetometer arrays. Phys. Med. Biol. 64, 21NT03. https://doi.org/10.1088/1361-6560/ab4c06
Nolte, G., 2003. The magnetic lead field theorem in the quasi-static approximation and its use for magnetoencephalography forward calculation in realistic volume conductors. Physics in Medicine and Biology 48, 3637–3652. https://doi.org/10.1088/0031-9155/48/22/002
Nunes, A.S., Kozhemiako, N., Moiseev, A., Seymour, R.A., Cheung, T.P.L., Ribary, U., Doesburg, S.M., 2020. Neuromagnetic activation and oscillatory dynamics of stimulus-locked processing during naturalistic viewing. NeuroImage 216, 116414. https://doi.org/10.1016/j.neuroimage.2019.116414
Osborne, J., Orton, J., Alem, O., Shah, V., 2018. Fully integrated standalone zero field optically pumped magnetometer for biomagnetism, in: Steep Dispersion Engineering and Opto-Atomic Precision Metrology XI. Presented at the Steep Dispersion Engineering and Opto-Atomic Precision Metrology XI, SPIE, pp. 89–95. https://doi.org/10.1117/12.2299197
Pakenham, D.O., Quinn, A.J., Fry, A., Francis, S.T., Woolrich, M.W., Brookes, M.J., Mullinger, K.J., 2020. Post-stimulus beta responses are modulated by task duration. NeuroImage 206, 116288. https://doi.org/10.1016/j.neuroimage.2019.116288
Park, H., Kayser, C., Thut, G., Gross, J., 2016. Lip movements entrain the observers' low-frequency brain oscillations to facilitate speech intelligibility. eLife 5, e14521. https://doi.org/10.7554/eLife.14521
Penfield, W., Boldrey, E., 1937. Somatic motor and sensory representation in the cerebral cortex of man as studied by electrical stimulation. Brain. https://doi.org/10.1093/brain/60.4.389
Pfurtscheller, G., Lopes da Silva, F.H., 1999. Event-related EEG/MEG synchronization and desynchronization: basic principles. Clinical Neurophysiology 110, 1842–1857. https://doi.org/10.1016/S1388-2457(99)00141-8
Pratt, E.J., Ledbetter, M., Jiménez-Martínez, R., Shapiro, B., Solon, A., Iwata, G.Z., Garber, S., Gormley, J., Decker, D., Delgadillo, D., Dellis, A.T., Phillips, J., Sundar, G., Leung, J., Coyne, J., McKinley, M., Lopez, G., Homan, S., Marsh, L., Zhang, M., Maurice, V., Siepser, B., Giovannoli, T., Leverett, B., Lerner, G., Seidman, S., DeLuna, V., Wright-Freeman, K., Kates-Harbeck, J., Lasser, T., Mohseni, H., Sharp, T.J., Zorzos, A., Lara, A.H., Kouhzadi, A., Ojeda, A., Chopra, P., Bednarke, Z., Henninger, M., Alford, J.K., 2021. Kernel Flux: a whole-head 432-magnetometer optically-pumped magnetoencephalography (OP-MEG) system for brain activity imaging during natural human experiences, in: Optical and Quantum Sensing and Precision Metrology. Presented at the Optical and Quantum Sensing and Precision Metrology, SPIE, pp. 162–179. https://doi.org/10.1117/12.2581794
Quinn, A.J., Atkinson, L., Gohil, C., Kohl, O., Pitt, J., Zich, C., Nobre, A.C., Woolrich, M.W., 2022. The GLM-Spectrum: A multilevel framework for spectrum analysis with covariate and confound modelling. https://doi.org/10.1101/2022.11.14.516449
Rhodes, N., Rea, M., Boto, E., Rier, L., Shah, V., Hill, R.M., Osborne, J., Doyle, C., Holmes, N., Coleman, S.C., Mullinger, K., Bowtell, R., Brookes, M.J., 2023. Measurement of Frontal Midline Theta Oscillations using OPM-MEG. NeuroImage 271, 120024. https://doi.org/10.1016/j.neuroimage.2023.120024
Roberts, G., Holmes, N., Alexander, N., Boto, E., Leggett, J., Hill, R.M., Shah, V., Rea, M., Vaughan, R., Maguire, E.A., Kessler, K., Beebe, S., Fromhold, M., Barnes, G.R., Bowtell, R., Brookes, M.J., 2019. Towards OPM-MEG in a virtual reality environment. NeuroImage 199, 408–417. https://doi.org/10.1016/j.neuroimage.2019.06.010
Robinson, S.E., Andonegui, A.B., Holroyd, T., Hughes, K.J., Alem, O., Knappe, S., Maydew, T., Griesshammer, A., Nugent, A., 2022. Cross-Axis Dynamic Field Compensation of Optically Pumped Magnetometer Arrays for MEG. NeuroImage 262, 119559. https://doi.org/10.1016/j.neuroimage.2022.119559
Roth, N., Küderle, A., Ullrich, M., Gladow, T., Marxreiter, F., Klucken, J., Eskofier, B.M., Kluge, F., 2021. Hidden Markov Model based stride segmentation on unsupervised free-living gait data in Parkinson's disease patients. Journal of NeuroEngineering and Rehabilitation 18, 93. https://doi.org/10.1186/s12984-021-00883-7
Sabo, A., Mehdizadeh, S., Iaboni, A., Taati, B., 2022. Estimating Parkinsonism Severity in Natural Gait Videos of Older Adults With Dementia. IEEE Journal of Biomedical and Health Informatics 26, 2288–2298. https://doi.org/10.1109/JBHI.2022.3144917
Schneider, S., Lee, J.H., Mathis, M.W., 2023. Learnable latent embeddings for joint behavioural and neural analysis. Nature 617, 360–368. https://doi.org/10.1038/s41586-023-06031-6
Schofield, H., Boto, E., Shah, V., Hill, R.M., Osborne, J., Rea, M., Doyle, C., Holmes, N., Bowtell, R., Woolger, D., Brookes, M.J., 2023. Quantum enabled functional neuroimaging: the why and how of magnetoencephalography using optically pumped magnetometers. Contemporary Physics 63, 161–179. https://doi.org/10.1080/00107514.2023.2182950

Sekihara, K., Nagarajan, S.S., Poeppel, D., Marantz, A., 2004. Asymptotic SNR of scalar and vector minimum-variance beamformers for neuromagnetic source reconstruction. IEEE Transactions on Biomedical Engineering 51, 1726–1734. https://doi.org/10.1109/TBME.2004.827926

Seymour, R.A., Alexander, N., Mellor, S., O'Neill, G.C., Tierney, T.M., Barnes, G.R., Maguire, E.A., 2021a. Using OPMs to measure neural activity in standing, mobile participants. NeuroImage 244, 118604. https://doi.org/10.1016/j.neuroimage.2021.118604

Seymour, R.A., Alexander, N., Mellor, S., O'Neill, G.C., Tierney, T.M., Barnes, G.R., Maguire, E.A., 2021b. Interference suppression techniques for OPM-based MEG: Opportunities and challenges. NeuroImage 118834. https://doi.org/10.1016/j.neuroimage.2021.118834

Shah, V.K., Wakai, R.T., 2013. A compact, high performance atomic magnetometer for biomedical applications. Phys. Med. Biol. 58, 8153–8161. https://doi.org/10.1088/0031-9155/58/22/8153

Sheng, D., Perry, A.R., Krzyzewski, S.P., Geller, S., Kitching, J., Knappe, S., 2017. A microfabricated optically-pumped magnetic gradiometer. Appl. Phys. Lett. 110, 031106. https://doi.org/10.1063/1.4974349

Singh, S.H., Peterson, S.M., Rao, R.P.N., Brunton, B.W., 2021. Mining naturalistic human behaviors in long-term video and neural recordings. Journal of Neuroscience Methods 358, 109199. https://doi.org/10.1016/j.jneumeth.2021.109199

Stangl, M., Maoz, S.L., Suthana, N., 2023. Mobile cognition: imaging the human brain in the 'real world.' Nat Rev Neurosci 1–16. https://doi.org/10.1038/s41583-023-00692-y

Thiede, A., Glerean, E., Kujala, T., Parkkonen, L., 2020. Atypical MEG inter-subject correlation during listening to continuous natural speech in dyslexia. NeuroImage 216, 116799. https://doi.org/10.1016/j.neuroimage.2020.116799

Tierney, T.M., Alexander, N., Mellor, S., Holmes, N., Seymour, R., O'Neill, G.C., Maguire, E.A., Barnes, G.R., 2021. Modelling optically pumped magnetometer interference in MEG as a spatially homogeneous magnetic field. NeuroImage 244, 118484. https://doi.org/10.1016/j.neuroimage.2021.118484

Tierney, T.M., Holmes, N., Meyer, S.S., Boto, E., Roberts, G., Leggett, J., Buck, S., Duque-Muñoz, L., Litvak, V., Bestmann, S., Baldeweg, T., Bowtell, R., Brookes, M.J., Barnes, G.R., 2018. Cognitive neuroscience using wearable magnetometer arrays: Non-invasive assessment of language function. NeuroImage 181, 513–520. https://doi.org/10.1016/j.neuroimage.2018.07.035

Tierney, T.M., Mellor, S., O'Neill, G.C., Timms, R.C., Barnes, G.R., 2022. Spherical harmonic based noise rejection and neuronal sampling with multi-axis OPMs. NeuroImage 258, 119338. https://doi.org/10.1016/j.neuroimage.2022.119338

Van Veen, B.D., Van Drongelen, W., Yuchtman, M., Suzuki, A., 1997. Localization of brain electrical activity via linearly constrained minimum variance spatial filtering. IEEE Transactions on Biomedical Engineering 44, 867–880. https://doi.org/10.1109/10.623056

Vidaurre, D., Quinn, A.J., Baker, A.P., Dupret, D., Tejero-Cantero, A., Woolrich, M.W., 2016. Spectrally resolved fast transient brain states in electrophysiological data. NeuroImage 126, 81–95. https://doi.org/10.1016/j.neuroimage.2015.11.047

Vivekananda, U., Mellor, S., Tierney, T.M., Holmes, N., Boto, E., Leggett, J., Roberts, G., Hill, R.M., Litvak, V., Brookes, M.J., Bowtell, R., Barnes, G.R., Walker, M.C., 2020. Optically pumped magnetoencephalography in epilepsy. Annals of Clinical and Translational Neurology 7, 397–401. https://doi.org/10.1002/acn3.50995

Weinreb, C., Osman, M.A.M., Zhang, L., Lin, S., Pearl, J., Annapragada, S., Conlin, E., Gillis, W.F., Jay, M., Shaokai, Y., Mathis, A., Mathis, M.W., Pereira, T., Linderman, S.W., Datta, S.R., 2023. Keypoint-MoSeq: parsing behavior by linking point tracking to pose dynamics. https://doi.org/10.1101/2023.03.16.532307

Westner, B.U., Dalal, S.S., Gramfort, A., Litvak, V., Mosher, J.C., Oostenveld, R., Schoffelen, J.-M., 2022. A unified view on beamformers for M/EEG source reconstruction. NeuroImage 246, 118789. https://doi.org/10.1016/j.neuroimage.2021.118789

Wilson, R.B., Enticott, P.G., Rinehart, N.J., 2018. Motor development and delay: advances in assessment of motor skills in autism spectrum disorders. Current Opinion in Neurology 31, 134. https://doi.org/10.1097/WCO.0000000000000541

Worsley, K.J., Friston, K.J., 1995. Analysis of fMRI Time-Series Revisited—Again. NeuroImage 2, 173–181. https://doi.org/10.1006/nimg.1995.1023

Yerys, B.E., Jankowski, K.F., Shook, D., Rosenberger, L.R., Barnes, K.A., Berl, M.M., Ritzl, E.K., VanMeter, J., Vaidya, C.J., Gaillard, W.D., 2009. The fMRI success rate of children and adolescents: Typical development, epilepsy, attention deficit/hyperactivity disorder, and autism spectrum disorders. Human Brain Mapping 30, 3426–3435. https://doi.org/10.1002/hbm.20767